

Investigation of pulsed laser induced dewetting in nanoscopic metal films: Thermal modeling and experiments

^{1,2}Justin Trice, ³Dennis Thomas, ^{1,2}Christopher Favazza,

^{2,3}Radhakrishna Sureshkumar, and ^{1,2}Ramki Kalyanaraman

¹*Department of Physics, Washington University in St. Louis, MO 63130*

²*Center for Materials Innovation, Washington University in St. Louis, MO 63130 and*

³*Department of Energy, Environmental and Chemical Engineering,*

Washington University in St. Louis, MO 63130

Pulsed laser-induced melting and dewetting of nanoscopic metal films have been used to assemble metal nanoparticles having spatial order and monomodal size distribution on SiO_2/Si substrates. Spatial pattern selection during dewetting determines the final particle size and inter-particle distance. Pattern selection and dynamical progression of interface disturbances are greatly dependent on parameters such as the energy threshold for laser melting (E_m), the liquid lifetime (τ_L), peak liquid temperature (T_L), rates of heating and cooling as a function of film thickness h and laser energy density E . Hence, we have developed a one dimensional lumped parameter heat transfer model applicable for the film thickness coupled with the heat equation for the substrate in the experimental regime in which $h < \text{laser absorption length } \alpha^{-1}$. The uniform film temperature is determined by E (which is allowed to vary with time) and heat loss to the substrate via conduction. However, since the substrate thickness is $>>$ the thermal diffusion length scale during the pulse, the heat transport in the substrate is explicitly modeled using the transient heat equation. In the limiting case of temperature-independent materials properties and timescale of melting $<<$ pulse time, analytical solutions are obtained. A finite element simulation was performed to relax the assumptions made in the analytic model to test their validity and, to include temperature-dependent materials parameters. The liquid lifetime estimated from the numerical solution agreed to within 20% with the analytic solution , while the peak temperature rise differed by $\sim 200\text{ K}$, primarily as a result of energy absorbed during the phase change not accounted for in the analytic model. Overall, theoretical predictions for E_m were consistent with experimental observations provided that thickness dependence of the reflectivity of the metal-substrate bilayer was taken into account . For small changes in laser energy density E above E_m , T_L and τ_L were found to increase linearly with increasing E . The heating and cooling rates were typically $\sim 150\text{ K/ns}$ and $\sim 4\text{ K/ns}$ respectively with liquid phase lifetimes of $2 - 15\text{ ns}$ in the experimental regime investigated. This is much smaller than the time scale associated with the growth of surface disturbances which, based on linear thin film hydrodynamic theory, is $\geq 25\text{ ns}$. Hence, dewetting would require the application of multiple pulses as seen experimentally. Using multiple pulse irradiation, the morphological evolution from an initially uniform Co film to a final robust state consisting of spatially ordered nanoparticles was experimentally investigated as a func-

tion of h , E and laser irradiation time, as measured by the number of pulses n . Pattern formation was typically characterized by the appearance of discrete holes followed by bi-continuous structures (for $h \leq 3 \text{ nm}$) or cellular patterns ($h \geq 3 \text{ nm}$) which finally evolved into nanoparticles. The nanoparticle length-scale characteristics were found to agree with the linear thin film hydrodynamic dewetting theory, with spacing $R \sim h^{1.98 \pm 0.2}$ and diameter $D \sim h^{1.5 \pm 0.2}$. We also studied the dependence of the final length scale R and the rate of pattern ripening on laser energy E . Because of the weak temperature dependence of the material parameters of Co, negligible changes in R were observed as a function of E while the rate of ripening had a simple linear dependence on laser E .

I. INTRODUCTION

Predictable and robust approaches to assemble metal nanoparticles with spatial order on insulating dielectric substrates like SiO_2 are important towards realizing various nanostructured applications, such as ordered field emission displays [1], high-density magnetic data storage [2, 3] and surface plasmon waveguides [4, 5]. Physical phenomenon that impose patterns with characteristic length scales are attractive for this purpose. One such class of phenomena are those exhibiting nonlinear dynamic instabilities with a robust stable state that is characterized by a narrow range of length scales. Typically such self-assembly of ordered patterns on surfaces and thin films arises from the competition between various effect. For example, surface rippling under ion irradiation is primarily due to an instability resulting from the competition between ion erosion and smoothing due to surface diffusion with the length and time scales determined by ion flux, surface temperature and surface diffusion parameters [6, 7, 8, 9, 10, 11, 12]. Alternately, nanopatterns could result from instabilities of a thin fluid film leading to spatial patterns with length and time scales that depend on the thermophysical material properties such as interfacial tension, contact angle with the substrate, fluid viscosity and, for ultrathin films, long range dispersion forces such as the van der Waal's interaction. An example for thin film pattern formation by such instabilities is that of spinodal dewetting, a hydrodynamic instability which occurs when attractive intermolecular forces exceed the stabilizing effect of interfacial tension [13, 14, 15, 16]. Under such conditions, film thickness fluctuations are spontaneously amplified leading to the breakup of the film and eventually to the formation of drops/particles with well defined spatial order [17].

Dewetting dynamics leading to particles have been studied in detail in polymer films that are in the liquid state close to room temperature [18, 19, 20, 21]. However, ordered nanoparticle formation via dewetting in metal films on insulating substrates has remained relatively unexplored primarily due to the high temperatures required to melt the metal and observe dewetting within practical time scales. The high melting temperature involved makes traditional heating approaches, like furnace annealing, inefficient. In this re-

gard, melting by energetic beams, which can provide sufficient intensities to selectively melt solid metal films on various substrates, is a promising tool to study liquid-phase dewetting in nanoscopic metal films. One example of such an approach is the work on ion-irradiation of ultrathin Pt films on SiO_2 substrates which resulted in dewetting patterns with spatial order [22, 23]. Another attractive energy source is a pulsed laser, which offers various pulse times, wavelengths and energy densities, making it an attractive processing tool. Approximately 10 years ago pattern formation following was investigated for melting by a *single* 7 ns laser pulse of thin films of various metals (Au, Cu, Ni) on a *Cr metal layer*, which, due to its much higher melting temperature, acted as an inert surface [24]. They found that the metal films (with thickness $h \geq 25$ nm) could be preferentially melted and their subsequent morphological changes depended upon the laser energy above the melting threshold (E_m). They explained the observed morphological changes as resulting from spinodal dewetting dynamics [25, 26]. However, such investigations pursuing the assembly of spatially ordered patterns under pulsed laser dewetting of metal films deposited directly on SiO_2 has not been pursued in great detail, especially in nanoscopic metal films with $h <$ the laser absorption depth α^{-1} .

Recently we have shown that *multiple ns* pulsed laser melting of nanoscopic Co films can lead to short- and long-range spatial order [27, 28, 29]. We also provided evidence that dewetting by multiple ns pulse laser melting shows characteristics of a thin film hydrodynamic (*TFH*) instability, such as the spinodal process [30]. This evidence was primarily based on the observation of the final nanoparticle morphology quantitatively described by the nearest-neighbour (*NN*) particle spacing (R) and diameter (D). The characteristics agreed with what would be predicted by a *TFH* theory modified to incorporate long range inter-molecular attractive forces of van der Waal's type. However, the role of various laser parameters, including, the energy and time measured implicitly by the number of pulses (n), and its role on the dewetting instability was not investigated in detail.

Understanding the role of pulsed laser parameters on the dewetting instability is important because of the temperature dependence of materials parameters and the strong transient thermal effects under the ns pulse irradiation that could result in changes to patterning dynamics and length scales. One approach to understand the laser response is to make experimental measurements of the heating, cooling, phase change, etc., during laser irradiation. While such measurements can be done routinely in macroscopic structures, nanoscopic metal films are more difficult to study simply because of the small scales involved. Another approach is to describe the heat transfer process mathematically in terms of the coupled conservation laws for energy for the film and the substrate along with the appropriate initial and boundary conditions. Pulsed laser heating and melting of thin films is a well-established field with numerous experimental, analytical and numerical confirmations of the laser-metal interactions on a wide variety of substrates [31, 32]. However, most of this work was concerned primarily with interaction of metal films of thickness comparable to or

larger than the absorption depth α^{-1} . An early attempt to provide an analytical solution to the thermal behavior of metal films with $h < \alpha^{-1}$ was provided by Matthias and co-workers [33]. However their solution for the melt threshold E_m was not tested against experimental measurements for length scales where $h < \alpha^{-1}$. Also, their analytical form was not used to predict liquid lifetimes τ_L or liquid temperature T_L . Recently, Henley and co-workers performed numerical modeling to determine E_m for melting of various metal films, including Ni, Au, Ag, Ti, Zn and Mo on SiO_2 substrates following irradiation by a 248 nm and 25 ns laser pulse [34]. They confirmed qualitatively the analytical prediction of Matthias et al., i.e. that the energy to melt the film increased with decreasing thickness below α^{-1} . However, they did not discuss the behavior for laser energies above E_m and so it was not possible to predict the liquid lifetime τ_L or the liquid temperature T_L , which are necessary towards understand the dewetting mechanisms and the role of laser parameters on the hydrodynamics of the dewetting process.

While numerical solution can be accomplished in a straightforward fashion using modern algorithms/computers, it fails to take advantage of certain simplifications that result from the nanoscopic nature of the film. Such simplifications, as shown in this work, allow us to derive insightful analytical solutions to the film temperature as a function of time. These simplifications include: (i) $h < \alpha^{-1}$; and (ii) the heat loss occurs primarily through conduction through the substrate so that the time-dependent film temperature may be considered to be uniform. Typically for pulse durations > 1 ns, Fourier heating theory is found to be applicable and consequently the laser heating may be described as a position-dependent source term in the transient energy equation [35]. Further, under the ultrafast heating rates, the phase change time scale for nanoscopic films is much smaller than that of the pulse duration. Under such conditions, we show that analytical solutions of heating by a 9 ns step and/or Gaussian pulse can be obtained for the heating and cooling rates if one assumes T-independent materials properties. Excellent quantitative agreement was found with the experimentally measured E_m . A linear dependence of T_L and τ_L was obtained for small changes in E above E_m for the entire range of h investigated. However, true experimental conditions of dewetting involve temperature-dependent material parameters and phase change and so we also relaxed the restrictions of T-independent parameters and obtained numerical solutions for the thermal behavior using finite element calculations [36]. The result for E_m and the trends in T_L and τ_L with E were similar to the analytical form. Quantitatively, the liquid lifetimes estimated from the analytical form were $\sim 20\%$ longer and the peak temperature rise was $\sim 200\text{ K}$ higher than the numerical values. *The good agreement between analytical predictions based on T-independent parameters and numerical estimates using T-dependent parameters suggests that for nanoscopic metal films with $h \leq \alpha^{-1}$ the analytical model is an adequate representation of the thermal behavior and can provide useful guidelines for parameter selection in experiments.*

Experimental studies of dewetting were performed on Co films on SiO_2 in the thickness range of

$h \leq \alpha^{-1} \sim 11 \text{ nm}$ for melting by a 9 ns pulsed laser operating at 266 nm and 50 Hz for various irradiation times n . These multiple instances of independent melting and resolidification were used to study the dynamical evolution of dewetting patterns as well as its behavior with laser energy density $E > E_m$. We determined that the dewetting process was characterized by short range order (SRO) at all observed stages of dewetting and that increasing the number of pulses progressed the dewetting instability to a final robust state of nanoparticles characterized by SRO in their nearest neighbour (NN) spacing R . Based on the predictions of the liquid lifetime and the observed trend of the spacing $R \sim h^2$ and the average particle diameter $D \sim h^{5/3}$, we suggest that the dewetting pathway is consistent with a *TFH* instability, similar to the spinodal dewetting instability, arising from competition between surface tension and long-range van der Waal's attractive forces [13, 14, 30]. Based on the analysis of the liquid lifetimes from the modeling we estimated that the dewetting time τ_D predicted from linear *TFH* theories [13] was much longer than τ_L for all film thickness and laser energies studied. This suggested that the rapid laser melting and resolidification could capture snapshots of the instability. Therefore, we suggest that once the dewetting is initiated by the melting, subsequent pulses continue to foster the instability. We also determined that changing the liquid temperature through laser energy did not have a measurable effect on the final length scale, and is consistent with the weak temperature-dependent behavior for Co. On the other hand, the pattern ripening rate, measured by the ratio of the observed dewetting length scale L over the irradiation time n increased linearly with E and/or T_L primarily as a result of the linear change in the liquid lifetime τ_L with E . These results emphasize that analytical models are extremely useful towards identifying dewetting mechanism following ns melting of nanoscopic metal films on SiO_2 substrates.

II. ANALYTICAL MODEL OF PULSED LASER HEATING AND COOLING

The thermal model was developed to simulate the experiment of heating by a pulsed laser beam incident normal to the film-substrate bilayer with a spatially uniform energy profile in the plane ($x - y$) of the bilayer that was infinitely wide in the x and y directions. For these conditions, the relevant heat diffusion was normal to the film surface in the z -direction where $z = -h$ corresponds to the vacuum-film interface and $z = 0$ the film-substrate interface. The model simulated a 1-D geometry consisting of a thin metallic layer on a thermally insulating substrate with the schematic shown in Fig. 1(a). The following assumptions were made in formulating the heat transfer expression:

1. The substrate layer is viewed as a semi-infinite medium in the downward z -direction. In the case of SiO_2 for UV irradiation, the substrate serves strictly as a conducting medium since it is transparent to UV.

2. The temperature T in the metallic nanolayer is spatially homogeneous in the z -direction; this is justified if the layer thickness is much smaller than the thermal diffusion length of the film.
3. The film is treated as continuous and planar with no surface deformation.

Let $T^*(z, t)$ be the film temperature. Then,

$$(\rho C_{eff})_m \frac{\partial T^*}{\partial t} = k_m \frac{\partial^2 T^*}{\partial z^2} + S_1^* f(t) \cdot \alpha_m \exp(-\alpha_m(z + h)) \quad (1)$$

where ρ is the density; C_{eff} is the effective heat capacity which also takes into account the effects of the phase change in the numerical model; k is the thermal conductivity (Note the subscript m denotes metal, s denotes the substrate); S_1^* is the rate of energy absorbed from the laser into the film; $f(t)$ denotes the temporal model of the laser; and α_m is the absorptivity of the metal film at 266 nm. For the case of constant heating, $f(t) = 1$; while $f(t) = 1 - H(t - t_p)$ for a square-shaped pulse where H is the Heaviside function; and $f(t) = e^{-\frac{(t-t_p)^2}{2\cdot\sigma^2}}$ for the Gaussian model. We are interested in the average film temperature especially since the spatial changes in T are expected to be small. An equation for $T \equiv \int_{-h}^0 T^* dz$ can be obtained by integrating the above equation from $z = -h$ to $z = 0$ and dividing throughout by h :

$$(\rho C_{eff})_m \frac{dT}{dt} = -\frac{q_s}{h} + \frac{S_1^* f(t)}{h} (1 - \exp(-\alpha_m h)) \quad (2)$$

where $q_s = -k_m (\partial T^* / \partial z)_0 = -k_s (\partial T_s / \partial z)_0$ is the conductive heat transfer to the substrate (T_s denotes substrate temperature). Note that the radiative heat transfer from the film surface to the vacuum is typically much smaller than the conductive transport to the substrate. Hence, $(\partial T^* / \partial z)_{z=-h}$ is set to 0. Thus, the lumped parameter equation is valid for all h given that T is interpreted as the average temperature in the film. Evidently, for $h < \alpha^{-1}$, the gradients would be sufficiently small so that this would be a good approximation to the uniform film temperature. Letting $S_1 = \frac{S_1^*(1 - \exp(-\alpha_m h))}{(\rho C_{eff})_m h}$, the time-dependent temperature in the metallic monolayer can be expressed as:

$$\frac{dT}{dt} = S_1 \cdot f(t) - \frac{q_s}{(\rho C_{eff})_m h} \quad (3)$$

where S_1 is the rate of energy absorbed from the laser, averaged over the film. For a Gaussian shaped pulse we have:

$$S_1^* = \left((1 - R(h)) \cdot \frac{E_o}{\sqrt{2 \cdot \pi} \cdot \sigma} \right) \quad (4)$$

and for constant heating or a square pulse

$$S_1^* = \left((1 - R(h)) \cdot \zeta \cdot \frac{E_o}{t_p} \right) \quad (5)$$

where R is the film thickness dependant reflectivity for the laser at normal incidence. The general expression for the effective R value for an absorbing film on a transparent substrate has been derived previously [37]. Fig. 1(b) presents the change in R for Co-SiO₂ over the film thickness range of interest; E_o is the laser energy density; σ is the standard deviation and was chosen so that the length of the Gaussian full-width half-maximum would be equal to the laser pulse width t_p ; ζ is a unit-less factor making the area underneath the square pulse equivalent to the area underneath the full-width half-maximum of the Gaussian temporal profile. Now applying energy balance conditions to the substrate, thermal diffusion may be formulated as:

$$\frac{\partial T_s}{\partial t} = \frac{k_s}{(\rho C_{eff})_s} \frac{\partial^2 T_s}{\partial z^2} + S_2 \cdot e^{-\alpha_s \cdot z} \quad (6)$$

with boundary conditions $T_s = T_o$ at $t = 0$; $T_s = T$ at $z = 0$ for $t > 0$; and $T_s = T_o$ as $z \rightarrow \infty$ for $t > 0$, which assumes a semi-infinite model for the substrate. S_2 is proportional to the power absorbed in the substrate per unit volume. Using the transformation $\Theta = T_s - T_o$, Eq. 6 can be written as:

$$\frac{\partial \Theta_s}{\partial t} = a_s \frac{\partial^2 \Theta_s}{\partial z^2} + S_2 \cdot e^{-\alpha_s \cdot z} \quad (7)$$

where a_s is given by $a_s = \frac{k_s}{(\rho C_{eff})_s}$ and with transformed boundary conditions $\Theta = 0$ at $t = 0$; $\Theta = T - T_o$ at $z = 0$ for $t > 0$; and $\Theta = 0$ as $z \rightarrow \infty$ for $t > 0$. The solution for Θ of Eq. 7 in the Laplace domain is expressed as follows:

$$\Theta(z, s) = \left(T(s) - \frac{T_o}{s} - \frac{S_2}{s(s - \alpha_s^2 \cdot a_s)} \right) \cdot e^{-\sqrt{\frac{s}{a_s}} z} + \frac{S_2 \cdot e^{-\alpha_s \cdot z}}{s \cdot (s - \alpha_s^2 \cdot a_s)} \quad (8)$$

For the case of constant heating, i.e. $f(t) = 1$, the Laplace transform of Eq. 3 is:

$$sT(s) - T_o = \frac{S}{s} - \frac{k_s}{(\rho C_{eff})_m h} \cdot \left(-\frac{\partial \Theta(z, s)}{\partial z} \Big|_{z=0} \right) \quad (9)$$

From Eq. 8 we have:

$$sT(s) - T_o = \frac{S}{s} - K\sqrt{s}T(s) + \frac{KT_o}{\sqrt{s}} + \frac{KS_2\sqrt{s}}{s(s - \alpha_s^2 a_s)} - \frac{KS_2\alpha_s\sqrt{a_s}}{s(s - \alpha_s^2 a_s)} \quad (10)$$

where $K = \frac{\sqrt{(\rho C_{eff} k_s)}}{(\rho C_{eff})_m h}$. Rearranging Eq. 10 and simplifying we find:

$$T(s) = \frac{S}{s^{3/2}(\sqrt{s} + K)} + \frac{T_o}{\sqrt{s}(\sqrt{s} + K)} + \frac{KT_o}{s(\sqrt{s} + K)} + \frac{KS_2}{s^{3/2}(\sqrt{s} + \alpha_s\sqrt{a_s}) \cdot (\sqrt{s} + K)} \quad (11)$$

Finally, for the constant heat source the resulting expression is:

$$\begin{aligned} T(t) = & T_o + \frac{2}{\sqrt{\pi}} \cdot \left(\frac{S_1}{K} + \frac{S_2}{\alpha_s\sqrt{a_s}} \right) \sqrt{t} + \frac{S_1}{K^2} \cdot \left(e^{K^2 t} \cdot \operatorname{erfc}(K\sqrt{t}) - 1 \right) \\ & - \frac{S_2}{\alpha_s^2 a_s K} \cdot \left(K + \alpha_s\sqrt{a_s} + \frac{K^2 \cdot e^{\alpha_s^2 a_s t} \operatorname{erfc}(\alpha_s\sqrt{a_s t})}{\alpha_s\sqrt{a_s} - K} - \frac{\alpha_s^2 a_s e^{K^2 t} \operatorname{erfc}(K\sqrt{t})}{\alpha_s\sqrt{a_s} - K} \right) \end{aligned} \quad (12)$$

However, in the interest of comparison with the experiments performed in this work on a transparent substrate (SiO_2), we can simplify the above expression by using $S_2 = 0$, indicating that there is no heat source within the substrate. To explore the heating and cooling dynamics of the bilayer system, we introduce the square pulse and Gaussian temporal profiles and solve for the thermal response. For the case of the square pulse, the Laplace transform of Eq. 3 for the metallic nanolayer is:

$$sT(s) - T_o = \frac{S \cdot (1 - \exp(-t_p \cdot s))}{s} - \frac{k_s}{(\rho C_p)_m h_m} \cdot \left(-\frac{\partial \Theta(z, s)}{\partial z} \Big|_{z=0} \right) \quad (13)$$

Combining equations 13 and 8, we have:

$$sT(s) - T_o = \frac{S \cdot (1 - \exp(-t_p \cdot s))}{s} - K\sqrt{s}T(s) + \frac{KT_o}{\sqrt{s}} \quad (14)$$

Rearranging Eq. 14 and further simplifying

$$T(s) = \frac{T_o}{s} + \frac{S}{s^{3/2}(\sqrt{s} + K)} - \frac{S \cdot \exp(-t_p \cdot s)}{s^{3/2}(\sqrt{s} + K)} \quad (15)$$

Finally, the inverse Laplace transform of Eq. 15 gives the solution for $T(t)$, i.e.,

$$T(t) = T_o + \frac{2}{\sqrt{\pi}} \cdot \left(\frac{S}{K} \right) \sqrt{t} + \frac{S}{K^2} \cdot \left(e^{K^2 t} \cdot \text{erfc}(K\sqrt{t}) - 1 \right) - S \cdot \int_0^t e^{K^2(t-u)} \cdot \text{erfc}(K\sqrt{t-u}) \cdot H(u-t_p) \cdot du \quad (16)$$

where the integral in Eq. 16 may be solved numerically. Now for the case of the Gaussian model, the Laplace transform of Eq. 3 for the metallic nanolayer is:

$$sT(s) - T_o = S' \cdot e^{\frac{(s-g)^2}{4 \cdot f^2}} \cdot \frac{\sqrt{\pi}}{2 \cdot f} \cdot \text{erfc}(\frac{s-g}{2 \cdot f}) - \frac{k_s}{(\rho C_p)_m h} \cdot \left(-\frac{\partial \Theta(z, s)}{\partial z} \Big|_{z=0} \right) \quad (17)$$

where $f = \frac{1}{\sqrt{2}\sigma}$, $g = 2 \cdot t_p \cdot f$, and $S' = S \cdot \exp(-f^2 \cdot t_p^2)$. Therefore Eq. 17 becomes:

$$sT(s) - T_o = S' \cdot e^{\frac{(s-g)^2}{4 \cdot f^2}} \cdot \frac{\sqrt{\pi}}{2 \cdot f} \cdot \text{erfc}(\frac{s-g}{2 \cdot f}) - K\sqrt{s}T(s) + \frac{KT_o}{\sqrt{s}} \quad (18)$$

Rearranging Eq. 18 and further simplifying

$$T(s) = \frac{T_o}{s} + \frac{S' \cdot e^{\frac{(s-g)^2}{4 \cdot f^2}} \cdot \frac{\sqrt{\pi}}{2 \cdot f} \cdot \text{erfc}(\frac{s-g}{2 \cdot f})}{\sqrt{s} \cdot (\sqrt{s} + K)} \quad (19)$$

Finally, the inverse Laplace transform of Eq. 19 gives the solution for $T(t)$, i.e.,

$$T(t) = T_o + S' \cdot \int_0^t \exp(-f^2 \cdot (t-u)^2 + g \cdot (t-u) + K^2 \cdot u) \cdot \text{erfc}(K\sqrt{u}) \cdot du \quad (20)$$

where the integral in Eq. 20 may be solved numerically using standard software packages. For both the Gaussian and square pulse solutions, we used the Riemann midpoint rule to evaluate the integral with MapleTM v9.1.

III. NUMERICAL SOLUTION

In order to validate the assumptions made in the analytic treatment, the complete modeled was solved using the finite element method via the commercial software FEMLabTM v3.1. Here, the assumption of homogeneous temperature in the film is relaxed. To mimic the semi-infinite condition for the substrate numerically, the boundary condition $T_s(z, t) |_{z=5 \cdot L_{th}} = T_o$ was imposed where L_{th} is the thermal diffusion length of the substrate given by $L_{th} = \sqrt{t_p a_s}$. The numerical simulations were performed for different meshes and time-steps till the solutions were consistent. For 1-D meshes with 5 or more nodes at the film geometry and scaled time-step ranging from $\Delta\tau \sim 0.1$ to 5 (where $\tau = \frac{t}{\beta \cdot t_p}$) the numerical solutions of the film temperature fell within 0.1%. For temperature independent parameters, we observed good agreement between the analytic and numerical calculations where variation between the two was less than 0.5 K (see Fig. 2(a)). First order phase transition was modeled via an effective heat capacity technique based on previous models [38, 39], namely:

$$C_{eff} = C_p + L \frac{\partial F}{\partial T} \quad (21)$$

where

$$F(T) = \begin{cases} \frac{T}{2\varepsilon} & \text{for } T_m - \varepsilon < T < T_m + \varepsilon \\ 0 & \text{otherwise} \end{cases} \quad (22)$$

L is the latent heat of transformation for the film; T_m is the melting temperature of the film. The functional form of $F(T)$ was chosen so that C_{eff} models a first order phase change, i.e. when $\frac{\partial F}{\partial T}$ is integrated from $T_m - \varepsilon$ to $T_m + \varepsilon$ the result equals unity. ε is a small temperature whose value was chosen so no oscillation would be observed during the melting and freezing phase of the simulation. A value of $\varepsilon = 15$ K was sufficient for simulations performed here. The quantitative values of the various materials parameters and temperature dependant expressions are tabulated in Table I. In addition, for all simulations, the thermal gradient in the numerical calculation from the film-surface to the film-substrate interface was $\ll 1$ K thereby validating the homogeneous film-temperature assumption.

IV. MODELING RESULTS

A. Effect of Laser Temporal Shapes

Equation 12 is consistent with the result obtained for bulk metal from [35] if we let $k_m = k_s$ and $S_2 = 0$. Also from Eq. 12, we note that for the heating portion where $t \gg \frac{1}{K^2}$ the temperature $T(t) \propto \sqrt{t}$ since $e^{K^2 t} \cdot erfc(K\sqrt{t})$ falls off very quickly. Upon introducing a scaling factor ζ so that the area underneath

the square pulse is equal to that of the Gaussian full-width-half-maximum, the Gaussian model still predicts a higher peak temperature for a given laser energy density. The input power for the Gaussian laser model peaks at a maximum while the square pulse is constant in time. Thus, power is still being input into the bilayer system even after the Gaussian beam begins to dissipate. At film thickness scales of $h < \alpha^{-1}$, the thermal transport into the substrate occurs very rapidly. When the laser input power shuts off (square-pulse case) or dissipates such that the input power is significantly overcome by the flux into the substrate (Gaussian case), the system quickly cools back to its initial state. Hence, the details of the instantaneous laser energy profile should be incorporated into the model to capture the laser energy melt-threshold and peak temperatures in agreement with experimental values. Hence, the analytic and numerical analysis that follow in this work are conducted using a Gaussian temporal shape.

B. Melt threshold

Fig. 2(a) shows a plot of Eq. 20 versus time for various Co film thicknesses h with a laser energy density value of $E = 100 \text{ mJ/cm}^2$. The points represent Eq. 20 solved at various time and the lines represent the respective finite element simulations. From thermal profiles of this type, the peak temperature and liquid lifetime were calculated as functions of h and E . In addition, from Eq. 20, the melt threshold energy E_m , which is the value of E needed to bring the Co film just to melting temperature was calculated. The time t_{max} where the maximum of Eq. 20 was first determined for the various film thicknesses. Then, Eq. 20 was set equal to T_m at $t = t_m$ and then solved for the appropriate value of E by successive approximations. The analytic melt threshold energy versus h is shown in Fig. 2(c) as the solid line along with the experimentally measured values (solid symbols) whose details are discussed in sec. VIA. In addition, Fig. 2(c) also presents the numerically predicted laser melt threshold energy density (dashed line). From Fig. 2(c), an increasing E_m with decreasing h is obtained for experiment and modeling and furthermore, the estimated E_m is in excellent agreement with experiment. From Eq. 3 one may show $\frac{dT}{dt} \propto \frac{q_s}{h}$ where q_s is the thermal flux contribution to the metal film from the substrate. Thus, for smaller films, the heat transfer to the substrate increases as $1/h$ resulting in a larger energy density value needed to overcome this contribution. In addition, modeling the role of the thickness dependence of the reflectivity for a metal film on a transparent substrate was paramount in acquiring good quantitative agreement with experiment, though overlooked in some analysis done in the past [40]. From Fig. 1(b), the thickness-dependent reflectivity of the bilayer system is presented from the value of bulk SiO₂ of $R \sim 0$ for $h_m = 0$ to the value of bulk Co of $R = 0.44$ [41]. In the thickness regime of interest, i.e. $h_m \leq 1/\alpha_m$, the calculated value is significantly smaller than that of bulk Co.

C. Liquid lifetime and temperature

From thermal profiles of the type shown in Fig. 2(a), the peak temperature and liquid lifetime were calculated as functions of h and E . Fig. 2(b) shows thermal profiles of the film temperature for various film thickness for a laser energy density value of $E = 125 \text{ mJ/cm}^2$. The liquid lifetime for the analytic model was defined by placing a line at $T_m = 1768 \text{ K}$, the Co melting temperature, and noting the time in between both intercepts. For the numerical model, the liquid life is defined as the time needed for the system to progress from the onset of melting to the completion of freezing. From Fig. 2(b) we see that introducing phase change into the model causes an appreciable change from the predicted temporal profile by Eq. 20. The portions of the figure where the temperature plateaus represent the film melting and freezing. Fig. 3(c) presents the liquid-life time and peak temperature versus laser energy density trends using the numerical and analytic models. From the figure, the numerical results (open symbols) predict liquid lifetimes about 20% lower than those predicted by the analytic model (closed symbols) for films greater than 1 nm. Also from Fig. 3(d), the peak temperatures predicted by the numerical model are lower by $\sim 200 \text{ K}$ than those predicted by the analytic model. Both these differences arise from the fact that the phase change in the numerical model consumes more energy and takes more time. Fig. 3(c) and (d) present the liquid lifetime and peak temperature as a function of laser energy density above the melt threshold for various film thicknesses. From thermal cycles of the type shown in Fig. 2, a linear relation was observed for the liquid life-time, $\tau_L(E, h) = A(h) \cdot E + B(h)$, and the peak temperature, $T_l(E, h) = C(h) \cdot E + D(h)$, for small changes in the laser energy density above E_m . In this laser energy density regime, the temperature of the Co film is above the melting temperature but below the vaporization temperature. The values for the coefficients A , B and C , D are presented in Tables II and III respectively.

D. Heating and cooling rates

Here, an order of magnitude calculation for the time needed for the bilayer system to rise to its peak temperature and the time needed for the system to cool to its initial temperature was estimated from the analytic solution (Eq. 20). First, plots of the type show in Fig. 2(a) were generated for Co film thickness of 1, 2, 3, 5, and 11 nm with laser energy density values chosen so that the peak temperature would be $\sim 2000 \pm 100 \text{ K}$. Next, the thermal cycle data was split into the heating and cooling portions. A linear fit $T(t, h) = P(h) \cdot t + Q(h)$ was applied to the heating portion (as show in Fig. 3(a) for the 3nm Co case) and a second order exponential fit $T(t, h) = U_1(h) \cdot \exp(-\frac{t}{t_1}) + U_2(h) \cdot \exp(-\frac{t}{t_2}) + v_o$ to the cooling portion (e.g. Fig. 3(b)). Tables IV and V present the fitted film-dependent coefficients for the heating and cooling

portion respectively. From the heating slope values $P(h)$, we see the typical rate of temperature rise of the bilayer system is $\sim 150 \text{ K/ns}$ for the metal-film thicknesses of interest. Thus, the system reaches its peak temperature $\sim 13 \text{ ns}$ after the onset of laser irradiation. From the time constant values for the cooling fit, we see that t_1 is consistently larger than t_2 and therefore dictates the rate at which the system will reach its final temperature. A second order fit gave the most accurate representation of the cooling portion. The two time constants result from: (i) the steady-state cooling of the system resulting from the energy balance condition Eq. 2 which gives t_1 ; and (ii) the residual energy input by the laser beam because of its Gaussian shape which gives t_2 . From Table V, $\sim 130 \text{ ns}$ is a typical value for t_1 . Thus, within approximately 500 ns the bilayer system will have reached 98% of its final value giving a time averaged cooling rate of $\sim 4 \text{ K/ns}$.

V. EXPERIMENTAL DETAILS

Cobalt metal films with thickness ranging from $1 \leq h \leq 8$ were deposited at rate of 1 nm/min onto optical quality SiO_2/Si substrates at room temperature. The substrates were commercially obtained with a 400 nm thick thermally grown oxide layer on polished $\text{Si}(100)$ wafers. Deposition was done under vacuum conditions ($2 \times 10^{-8} \text{ Torr}$) by e-beam evaporation from a TECTRA e^- -flux mini electron-beam evaporator. The wafers were degreased in acetone, methanol, and DI water prior to film deposition. The film thickness was controlled through the deposition rate as measured using an in-situ Inficon XTM/2 deposition monitor. The final thickness was established by calibrating concentration measurements of Co film using energy dispersive x-ray spectrometry (EDS) in a scanning electron microscope (SEM) to measurements by Rutherford backscattering [42, 43]. During each deposition run, up to 8 pieces of the substrate measuring approximately $5 \times 5 \text{ mm}^2$ were placed such that a number of different irradiation experiments could be performed in vacuum. The thickness variation between the different pieces in a single run was measured to be less than 10%. For every film thickness we also made atomic force measurements (AFM) of the surface roughness and an upper limit of $0.1 \pm .03 \text{ nm}$ was established for average rms roughness over the entire film thickness range. AFM was performed in ambient conditions using a Molecular Imaging PicoScan AFM with a tip of spring constant 0.2 N/m . The measured lateral ($x - y$) resolution was $\sim 10 \text{ nm}$ and z -height resolution was $\sim 0.2 \text{ nm}$. A Hitachi S-4500 field-emission microscope operating at 15 kV was used for EDS and SEM measurements. The spatial resolution of this microscope was $\sim 1.5 \text{ nm}$.

The films were irradiated in vacuum at normal incidence by a laser beam of variable beam size controlled by a 500 mm biconvex lens, with a maximum size of $3 \times 3 \text{ mm}^2$. The laser used was a Spectra Physics Injection seeded Lab-130-50 Nd:YAG laser operating at its 4th harmonic with wavelength $\lambda = 266 \text{ nm}$ at 50 Hz repetition rate. Based on the result of the modeling (Sec. IV D) the metal film returned to room

temperature within approximately 500 ns and therefore each laser pulse could be viewed as being thermally independent. The laser beam was plane polarized with a coherence length of $\sim 2\text{ m}$ and had a Gaussian temporal shape. The pulse width τ_p , as measured by the full-width-half-maxima of the temporal profile, was 9 ns . The spatial profile of the beam was a circular multimode energy distribution established by the diffraction output coupler of this laser. The spatial energy distribution was best described by fitting to a Gaussian shape which gave a 85% fit to the centroid of the distribution in each direction with a FEM of 4 mm . In the studies reported here, all morphology investigations were reported from an approximately $50 \times 100\text{ }\mu\text{m}^2$ region of the irradiated area within which the laser energy density variation was $\leq 20\%$ in each of the two dimensions.

Two types of laser irradiation experiments were performed. The first was determination of the melt threshold laser energy density, E_m . We defined E_m as the minimum energy density at which a morphology change could be detected after irradiation by 10,500 laser pulses. The morphology change observed was a large surface deformation visible under scanning electron microscopy (SEM) studies. Such an approach has been successfully used in the past to detect melt threshold of thin films under laser irradiation [33]. The laser energy density was controlled by varying the lens-sample position and/or the laser energy, which was measured using an Ophir electronics *PE30 A-P* high-power laser detector head with an ORION power meter. In this manner energy densities ranging from $10 - 1000\text{ mJ/cm}^2$ could be achieved. The second study was of dewetting pattern evolution as a function of various energy densities $E \geq E_m$ and over a range of irradiation times, as measured by the number of pulses n . The irradiation time typically ranged from $10 \leq n \leq 10500$. The pulse number was controlled by a shutter in the beam path. Each independent irradiation, i.e. with a different E and/or n were performed on different pieces of the substrate and each was characterized using SEM and/or AFM measurements. While the lower limit on the choice of E was set by E_m , the upper limit was set by ensuring that after the longest irradiation times no substantial evaporation ($\leq 10\%$) had occurred. This was ensured by measuring the concentration of metal after irradiation via EDS in the SEM and comparing with the thickness calibration values. In this manner detailed information on pattern formation was obtained as a function of E and n for each h under conditions not influenced by evaporation.

VI. EXPERIMENTAL RESULTS AND DISCUSSION

A. Laser energy threshold E_m to observe dewetting vs thickness (E_m)

The morphology of the films were first investigated as a function of increasing laser energy density over a practical time scale ranging from a few laser pulses to a maximum of $10.5K$ laser pulses. The first observation was that below a critical E no morphology change could be observed even after the longest irradiation. On the other hand, above this energy, significant morphology changes could be observed even after the shortest irradiation time. The morphology change used here was any detectable change to the film surface under high-magnification SEM imaging. Using this approach, a measurable critical E was obtained for a variety of film thickness. This critical energy was designated the melt threshold E_m and its behavior with h is plotted in Fig. 2(c). Very good agreement was observed for the experimentally observed values to the predictions of E_m using the models, as shown in the figure. The observed trend, i.e. a significant increase in E_m with decreasing h for the ultrathin films ($h \leq 5 \text{ nm}$) is consistent with the prediction of [33] as well our analytical and numerical models. Based on this quantitative agreement between the models and experiment, we interpreted this critical energy to be the melt threshold energy and all subsequent dewetting behavior was investigated for energies above the E_m for the various h .

B. Dewetting pattern evolution with n and E

A detailed investigation of the dewetting morphology was performed for various laser energies as a function of the laser irradiation time n . For films in the range of $3 \leq h \leq 7 \text{ nm}$ the the patterns typically consisted of discrete holes at the early stages of irradiation, followed by cellular patterns at later stages and eventually nanoparticles which remained stable to irradiation. On the other hand, for the films with $h < 3 \text{ nm}$, the morphology consisted of discrete holes followed by a bi-continuous structure with a final state again characterized by nanoparticles. It is widely accepted that the dewetting morphology can arise from three mechanisms [44]. (i) Homogeneous nucleation and growth in which holes appear randomly in location and time on the surface. Therefore, no characteristic length is present in this type of dewetting [20]. (ii) Heterogeneous nucleation and growth due to defects, impurities or other experimentally imposed heterogeneities. Here, a characteristic length scale could appear at the early stages of dewetting due to ordered nucleation sites. For instance, in ion-irradiation induced dewetting, the average molten zone of an ion imposes a characteristic length scale in dewetting [23]. (iii) Thin film hydrodynamic (T.F.H.) instabilities such as the one associated with the dewetting of spinodally unstable systems. The resulting patterns are characterized by a well-defined length scale in the hole spacing and/or size [19]. Since we have ruled

out spatially ordered heterogeneities on the surface and in the film microstructure, the results presented below were analyzed to distinguish between dewetting by homogeneous nucleation and *TFH* instabilities, such as spinodal dewetting, that establish a characteristic length scale. In order to do this, the primary characterization used was analysis of the power spectrum (*PS*) of the dewetting morphologies from which an understanding of the characteristic spatial frequencies in the patterns could be evaluated.

1. Dewetting morphology for $h < 3 \text{ nm}$

Fig. 4(a) to (d) captures the morphology of a 2 nm thick Co film as a function of increasing number of laser pulses at energy 200 mJ/cm^2 . Discrete holes are visible after the shortest time (Fig. 4(a)) with the patterns changing to a bi-continuous structure (Fig. 4c and d) and finally into nanoparticles (Fig. 4(d)). As shown in Fig. 7(a), the nanoparticles have a monomodal size distribution. The spatial nature of the patterns could be understood by performing fast Fourier transforms (*FFT*) to obtain the power spectrum (*PS*), as shown in Fig. 4(a) to (d). During all observed stages of the pattern evolution an annular shaped *PS* was visible, suggesting that a band of characteristic spatial frequencies was present in the patterns. Qualitatively, the radius of the annular region changed with increasing irradiation time reflecting the change in morphology of the dewetting patterns. Fig 5(a) to (d) show the pattern morphology after 100 pulses as a function of various energies for the 2 nm film. The general characteristics of the morphology were similar to those observed as a function of n , as shown in Fig. 4 and the primary role of increasing energy appears to be an enhanced rate of achieving the nanoparticle state.

2. Dewetting morphology for $3 \leq h \leq 7 \text{ nm}$

For the thicker films the intermediate stages of dewetting differed considerably in their morphology from Fig. 4 but still retained a characteristic spatial frequency. Fig. 6(a) to (d) captures the morphology of a 4.4 nm thick Co film as a function of increasing number of laser pulses at energy 93 mJ/cm^2 . Discrete holes are visible after the shortest time (Fig. 6(a)) with the patterns changing to a cellular structure (Fig. 6(c)) as the number of holes increases. Continued irradiation results in the metal being pushed to the edge of the holes and the patterns consisted of large polygonal structures with evidence for particle formation occurring preferentially at the vertices. This is more evident in Fig. 6(c). After long irradiation times, the stable nanostructure morphology is observed (Fig. 6(d)). Analysis of the *PS* for each pattern again showed an annular structure indicating spatial order in the dewetting patterns, as shown in figures 6(a) to (d). The radial distribution function $g(k)$ for each of these *PS* and the curve fitting to obtain L are

shown in Fig. 8(a). The cumulative behavior of L vs n for this film is shown in Fig. 8(b). As in the case of the 2 nm film, L increases as the holes appear and merge to form closed ring-like polygons. In this scenario, L represents the average diameter of the holes or polygons. However, unlike the case of 2 nm film, the appearance of the nanoparticles decreases the characteristic length scale. This can be understood by noting that now L represents the average NN spacing of the nanoparticles which formed preferentially at the vertices of the polygons. Since the average vertex spacing is smaller than the average diameter of the polygons so L decreases as polygons change into nanoparticles. The nanoparticles once again have a monomodal size distribution, as shown in Fig. 7(b). We also investigated the role of laser energy on the pattern formation and similar to the case of the 2 nm film observed that once again the primary effect of increasing energy is an enhanced rate of achieving the nanoparticle state. This effect is better represented in Fig. 8(b) where the characteristic L determined from the $g(k)$ is plotted as a function of n for various laser energies E . As the laser energy increases, the observed value of L is larger suggesting that the dewetting rate increases. However, the final L which represents the nanoparticle morphology after long irradiation times is independent of the laser E . This result once again confirms that the final nanoparticle state is extremely robust to the laser parameters.

3. Quantitative evidence for TFH instability

From the above results we suggest that the pulsed laser melting initiates the nonlinear dewetting TFH instability and subsequent pulses evolve this instability to a well-defined final state. Further, each observed state is characterized by a narrow band of spatial frequencies indicating spatial order over the entire dewetting process. Since we can rule out heterogeneous nucleation from ordered surface defects, the above results point strongly to dewetting by an instability. A more quantitative evidence for this TFH instability can be pursued on the basis of predictions of the linear theory in which the characteristic time scales and length scales of dewetting are well-defined functions of h . From our previous results, the most robust measure of the dewetting length scale appears to be the final nanoparticle state [30]. Therefore, we performed a study of the characteristics of this final nanoparticle state including, R , D , contact angle function $f(\theta)$ and the particle areal density N as a function of film thickness h to determine pattern formation via the TFH instability. From these measurements, we were also able to validate that the dewetting time scale is much larger than the liquid lifetime for each pulse, and hence pattern formation via the instability could be supported in such multiple pulse experiments.

1. R vs h

In the linear approximation of the *TFH* instability, the characteristic spinodal length Λ as a function of film thickness can be expressed as [13, 15, 17, 30]:

$$\Lambda(h) = \sqrt{\frac{16\pi^3\gamma}{A}}h^2 = Bh^2 \quad (23)$$

where γ is the surface tension of the metal and A is the Hamaker constant. Since we interpret the final nanoparticle morphology as resulting from the dewetting instability, we assigned the observed *NN* spacing R to be proportional to Λ as $R = a\Lambda$, where a is the proportionality factor. This is reasonable given that the average nanoparticle spacing is related to the average size and/or spacing between the ordered features arising from the dewetting process. We determined the behavior of R as a function of film thickness, as shown Fig. 9(a). The power law fit to the spacing R yielded a behavior expressed by $R(nm) = 25.7h^{1.98\pm0.3}$ with the film height expressed in nm. The *NN* spacings varied from ~ 40 to 1000 nm for the films studied. The exponent of the film thickness of 1.98 ± 0.3 is in excellent agreement to the theory value of 2. From this experimentally established pre-exponential factor of 25.7 nm^{-1} the Hamaker constant was estimated to be $A = 14.1 \times 10^{-19}\text{ J}$ which is of the right order of magnitude [45].

2. Dewetting instability time scale τ_D

In this multiple pulse laser melting dewetting scenario, the morphology change occurs over multiple cycles of phase change, i.e. melting and resolidification. Clearly, once the instability is initiated, in order for it to be fostered by the multiple pulses, the time scale of dewetting τ_D must be larger than the lifetime of the liquid τ_L in each pulse. From the linear theory, τ_D can be expressed as:

$$\tau_D(h) = \frac{96\pi^3\gamma\eta}{A^2}h^5 \quad (24)$$

where $\eta = 4.46 \times 10^{-3}\text{ Pa}\text{--s}$ is the viscosity of liquid Co at its melting point. Using the experimentally determined value of A we find that $\tau_D \sim 25\text{ ns}$ for a 1 nm thick film and increases as h^5 . From our modeling, we determined that at the melt threshold of $\sim 338\text{ mJ/cm}^2$ for the 1 nm film, the liquid lifetime is $\sim 4\text{ ns}$. In general the liquid lifetime for the range of films studied here varied between 4 to 15 ns, as determined from the model, and clearly is smaller than the dewetting time estimated from Eq. 24. Therefore, the experimental and modeling results support dewetting via the *TFH* dewetting instability.

3. D and $f(\theta)$ vs h

An analytical relation between the diameter of a particle D and the *NN* spacing R can be derived based on volume conservation [18]. Assuming that a circular section of the film with a volume

approximated as a cylinder of diameter R and thickness h contributes to one spherical nanoparticle of diameter D , then volume conservation suggests that:

$$\frac{\pi}{4}R^2h = \frac{4\pi}{3}f(\theta)\frac{D^3}{8} \quad (25)$$

where $f(\theta)$ is the geometric factor based on the particle contact angle θ that determines the fraction of the sphere that lies above the substrate (for the case of $\theta = 180^\circ$, $f(\theta)=1$). Using the characteristic length from Eq. 23 in Eq. 25 we get:

$$D = \left(\frac{24\pi^3\gamma}{Af(\theta)}\right)^{1/3}h^{5/3} = Ch^{5/3} \quad (26)$$

In Fig. 9(b) the average particle diameter D is plotted as a function of h . D varied from ~ 30 to 250 nm for the thickness range studied here. The power-law fit to our experimental data gives $D(\text{nm}) = 14.8h^{1.6\pm0.3}$ with the film height expressed in nm. The exponent of 1.6 ± 0.3 is in excellent agreement with the theoretical estimate of $5/3 = 1.67$. By using the experimentally determined pre-exponent of $14.1\text{ nm}^{-2/3}$ in Eq. 26, we determined the geometric factor to be $f(\theta) = 0.361$ giving an effective contact angle for the nanoparticles of 74° . Given the simplicity of the model relating the instability length scale to the particle diameter and the uncertainties in the values of R and D of approximately 30%, this experimentally extracted value of the contact angle could be said to be in reasonable agreement to the previously reported value of $100 \pm 26^\circ$ measured by atomic force and scanning electron microscopy [29].

4. Areal density N vs h

The areal density N of particles can be defined as:

$$N = 1/\left(\frac{\pi}{4}\Lambda^2\right) \quad (27)$$

which using Eq. 23 results in a thickness dependence given by:

$$N(h) = \frac{A}{4\pi^4\gamma}h^{-4} \quad (28)$$

Plotted in Fig. 9(c) is the variation in the observed particle density with h . A power law fit gives $N = 1.5 \times 10^{-3}h^{-3.8\pm0.8} \#/\text{nm}^2$ with the film height expressed in nm. The exponent of -3.8 ± 0.8 is in fair agreement with the expected value of 4 (with the uncertainty primarily arising from propagation errors in the various quantities) while the pre-exponent is consistent with the value obtained by substituting the experimentally determined A and γ in Eq. 28.

From these quantitative results, a *TFH* dewetting instability, like spinodal dewetting, appears to be a suitable explanation of the pattern formation in these nanoscopic Co films. The break-up of the polygonal structures in Fig. 6 into the particles requires some elaboration. Previous studies of break-up of cellular structures made from polygons into droplets have attributed the process to a Rayleigh instability due to which the particle diameter will follow the trend $D \sim h^{3/2}$ [18, 34]. However, we argue that particle formation in this work is a continuation of the dewetting process. The primary evidence is that the nanoparticles predominantly form at the junctions of the polygons, as compared to the classic string-like particle distribution resulting from the Rayleigh instability of the polygon sides.

VII. ROLE OF CO LIQUID TEMPERATURE AND LIFETIME ON DEWETTING

From the experiment results of dewetting presented in the previous section, the length scales L during the early stages of dewetting increase with increasing laser energy following similar irradiation times (Fig. 8). From our modeling, increasing laser energy increases the Co liquid temperature and the liquid lifetime. Further, the length scale of dewetting, Λ and the dewetting timescale τ_D have temperature-dependent materials parameters (i.e. γ and η). Therefore the observations of Fig. 8 can arise from three factors: (i) from a change in the dewetting length scale Λ ; (ii) from an increase in liquid lifetime τ_L per pulse; and (iii) from a change in the time scale for ripening τ_R of the dewetting structures. However, Fig. 8 also indicates that changing the laser energy has no influence on the final nanoparticle characteristic, implying that no permanent change to Λ must occur with change in liquid T_L . In this section we show that the change in Λ for Co metal is experimentally indistinguishable over significant T changes (of up to 500 K above T_m). From theoretical arguments we find that the increase in L with increasing E following irradiation by a small number of pulses n (i.e. early stages) comes from modifications to τ_L and τ_R and a quadratic behavior with E . This result was also consistent with our experimental observations based on the measurement of L vs n for various energies and thickness.

A. Role of temperature on Λ

The T-dependence of the dewetting length Λ , which comes from the surface tension $\gamma(T)$ and the Hamaker constant $A(T)$, can be expressed as:

$$\Lambda(h, T) = \sqrt{\frac{16\pi^3\gamma(T)}{A(T)}h^2} \quad (29)$$

The variation in temperature can be expressed as:

$$\frac{d\Lambda}{dT} = \sqrt{16\pi^3} \left[\frac{1}{2A^{1/2}} \gamma^{-1/2} \frac{\partial\gamma}{\partial T} - \frac{\gamma^{1/2}}{2A^{3/2}} \frac{\partial A}{\partial T} \right] h^2 \quad (30)$$

Eq. 30 can be simplified for metals on SiO_2 system by noting that the Hamaker constant for metals is virtually independent of temperature [46] and so $\frac{\partial A}{\partial T} \sim 0$ resulting in:

$$\frac{d\Lambda}{dT} = \sqrt{16\pi^3} \left[\frac{1}{2A^{1/2}} \gamma^{-1/2} \frac{\partial\gamma}{\partial T} \right] h^2 \quad (31)$$

For a temperature rise of ΔT over the melting point, the change in length can be expressed as:

$$\Delta\Lambda(\Delta T) = \frac{\Lambda(T_m)}{2\gamma(T_m)} \frac{d\gamma}{dT} \Delta T = -2.66 \times 10^{-4} \Lambda(T_m) \Delta T \quad (32)$$

where $\Lambda(T_m)$ is the length at the melt temperature and $\gamma(T_m)$ and $d\gamma/dT$ for Co are taken from Table VI. From this we see that Λ decreases as T_L increases, but this decrease is small and for temperature rises of up to $\Delta T = 500 \text{ K}$ is only $\sim -13\%$. This change is smaller than the spread in the experimental values of R of $\pm 20\%$ as measured from the $g(k)$. Therefore, for conditions under which the Co liquid T rise is $\sim 500 \text{ K}$ above T_m the change in length scale will be experimentally indistinguishable.

B. Role of T on ripening rate L/n

Within the linear theory of dewetting via a TFH instability the pattern ripening time τ_R is expected to be proportional to the dewetting time τ_D [13] and so we can express the T-dependent ripening time as:

$$\tau_R(h, T) = \omega \tau_D = \omega \frac{96\pi^3 \gamma(T) \eta(T)}{A(T)^2} h^5 \quad (33)$$

From this we can also define the ripening rate as $\sigma \propto \frac{\Lambda}{\tau_R}$, which can be evaluated using Eq. 29 and 33 as:

$$\sigma(h, T) = \kappa \frac{\Lambda(h, T)}{\tau_R(h, T)} = M \gamma(T)^{-1/2} \eta(T)^{-1} A^{1/2} h^{-3} \quad (34)$$

where $M = \frac{\kappa}{\omega} \frac{\sqrt{16\pi^3}}{96\pi^3}$ is a proportionality constant with unknown numerical factors of κ and ω . Using these expressions, the experimentally observed dewetting length L for a film of thickness h at a given laser energy $E > E_m$ following irradiation by n pulses can be expressed as:

$$L(h, E, n) = \sigma(h, E) \tau_L(E, h) n \quad (35)$$

where τ_L , the lifetime of the liquid, is a function of the laser energy and film thickness. In order to evaluate the expected behavior, each of the temperature (and laser E) dependent terms on the rhs can be evaluated:

1. Behavior of ripening rate $\sigma(h, T)$ for Co:

The temperature dependence of σ can be expressed analytically as:

$$\frac{d\sigma(T, h)}{dT} = -B \frac{A^{1/2}}{\gamma^{1/2} \eta} h^{-3} \left[\frac{1}{2} \frac{\gamma_T}{\gamma} + \frac{\eta_T}{\eta} \right] \quad (36)$$

where, $\gamma_T = \frac{\partial \gamma}{\partial T}$ and $\eta_T = \frac{\partial \eta}{\partial T}$ and the temperature dependence of the Hamaker constant has been neglected. The behavior of $\sigma(T)$ with temperature can be evaluated for Co metal by using the materials parameters from Table VI. Fig. 10(a) shows that Eq. 36 is well described by a linear behavior which increases with increasing temperature of the form:

$$\sigma(T, h) = \beta A^{1/2} h^{-3} [0.29T - 350] = \sigma_T(h)T - \sigma_o(h) \quad (37)$$

2. Dependence on liquid T and lifetime τ_L on E:

From the numerical results obtained in sec. IV D, the T and τ_L increased linearly with E for the various film thickness. Therefore, these quantities can be expressed as:

$$\tau_L(E, h) = A(h)E - B(h) \quad (38)$$

$$T_L(E, h) = C(h)E + D(h) \quad (39)$$

where the slopes A and C and intercepts B and D are thickness dependent positive quantities. In Table II and III, the parameters of the fits obtained from the numerical modeling of the thermal behavior are given.

Using Eq. 38 in Eq. 35 and Eq. 39 in Eq. 37 we can express the rate of change of dewetting length L with n as:

$$\frac{L(E, h)}{n} = pE^2 + qE + r \quad (40)$$

where $p = \sigma_T C A$; $q = \sigma_T (D A - B C) - \sigma_o A$; and $r = -B(\sigma_T D - \sigma_o)$ are the resulting temperature and thickness coefficients. Equation 40 can be further simplified by analysing the magnitudes of the various coefficients using typical numbers from Tables II and III. For example, for films in the range of 1 to 11 nm at the melting point of Co, the coefficient $p \ll q$ and the quadratic term in Eq. 40 can be dropped to give:

$$\frac{L(E, h)}{n} = qE + r \quad (41)$$

Therefore the experimentally observed trend in the ripening rate with laser energy should be linear. As shown in Fig. 10(b), the L/n for for various film thickness can be described by linear fits (dashed lines). The physical significance of this linear behavior is primarily because of the weak temperature dependence of the material parameters of Co. Therefore the primary contribution to the ripening rate due to increasing energy is the increasing lifetime of the liquid, which as shown in Fig. 3(c), varies linearly with E.

VIII. SUMMARY AND CONCLUSIONS

In conclusion, we have investigated the thermal and dewetting behavior of nanoscopic Co metal films with thickness $h < \alpha^{-1}$ on thermally insulating SiO_2 substrates following multiple ns pulse laser irradiation using 266 nm UV light. We developed an analytical and numerical model based on 1-D heat transport to describe the heating, cooling and liquid behavior as a function of film thickness h and laser energy density E . Both models provided excellent agreement with experimental measurements of energy threshold for laser melting (E_m) provided the thickness dependent reflectivity of the metal-substrate system was used. The analytic model agreed well with numerical calculations of the liquid-lifetime for films $> 1 \text{ nm}$. The liquid lifetime (τ_L) and peak liquid temperature (T_L) were found to increase linearly with small changes in laser energy above the E_m . The typical heating and cooling rates were $\sim 150 \text{ K/ns}$ and $\sim 4 \text{ K/ns}$ respectively. Experimental measurements of dewetting were made under multiple pulse laser irradiation of the Co films. Since the estimated cooling time following irradiation by a single pulse of $\sim 500 \text{ ns}$ was much smaller than the time between pulses of 20 ms each pulse was thermally independent. Under these conditions pattern formation as a function of increasing number of laser pulses was characterized by the appearance of discrete holes followed by bi-continuous structures (for $h < 3 \text{ nm}$) or cellular patterns ($h \geq 3 \text{ nm}$) which finally evolved into nanoparticles. During every stage of dewetting, ordering in size or spatial distribution was observed. Estimates of the liquid lifetimes from the numerical model, of 4 to 15 nm for the entire range of h and E investigated, indicated that the lifetimes were smaller than the spinodal time. The experimentally determined nanoparticle spacing varied as $R \sim h^{1.9 \pm 0.2}$ and diameter as $D \sim h^{1.6 \pm 0.2}$. Based on this temporal and spatial property of the patterns, the mechanism for dewetting is likely a thin film hydrodynamic instability, similar to spinodal dewetting. We also found that the nanoparticle nearest-neighbour spacing R was unchanged with laser energy E while the rate of ripening had a linear dependence on laser E . This behavior was primarily because of the weak temperature dependence of the material parameters of Co and the linear dependence of the liquid lifetime on laser energy. These results show that analytical models can be used to provide critical information on liquid lifetime and peak temperature, on the basis of which dewetting mechanisms can be identified.

RK acknowledges support by the National Science Foundation through a CAREER grant # DMI-0449258. JT acknowledges valuable conversations with Dr. Massoud Javidi in regards to the phase-change portion of the numerical model. RS and DT acknowledge NSF grant CTS 0335348.

[1] S. Fan, M. Chapline, N. Franklin, T. Tombler, A. Cassell, and H. Dai, *Science* **283**, 512 (1999).

- [2] R. White, *J. Mag. Magn. Mat.* **209**, 1 (2000).
- [3] S. Sun, C. Murray, D. Weller, L. Folks, and A. Moser, *Science* **287**, 1989 (2000).
- [4] M. Quinten, A. Leitner, J. Krenn, and F. Aussenegg, *Optics Lett.* **23**, 1331 (1998).
- [5] S. Maier, P. Kik, H. Atwater, S. Meltzer, E. Harel, B. Koel, and A. Requicha, *Nature Materials* **2**, 229 (2003).
- [6] P. Sigmund, *J. Mat. Sci.* **8**, 1545 (1965).
- [7] R. Bradley and J. Harper, *J. Vac. Sci. Tech. A* **6**, 2390 (1988).
- [8] E. Chason, T. M. Mayer, B. K. Kellerman, D. T. McIlroy, and A. J. Howard, *Phys. Rev. Lett.* **72**, 3040 (1994).
- [9] J. Erlebacher, M. J. Aziz, E. Chason, M. B. Sinclair, and J. A. Floro, *Phys. Rev. Lett.* **82**, 2330 (1999).
- [10] S. Facsko and H. Kurz, *Phys. Rev. B* **63**, 165329 (2001).
- [11] R. Moroni, D. Sekiba, F. B. de Mongeot, G. Gonella, C. Boragno, L. Mattera, and U. Valbusa, *Phys. Rev. Lett.* **91**, 167207 (2003).
- [12] M. Xu and C. Teichert, *J. Appl. Phys.* **96**, 2244 (2004).
- [13] A. Vrij, *Discuss. Faraday Soc.* **42**, 23 (1966).
- [14] A. Sharma and E. Ruckenstein, *Langmuir* **2**, 480 (1986).
- [15] A. Sharma, *Langmuir* **9**, 861 (1993).
- [16] R. Seemann, S. Herminghaus, and K. Jacobs, *Phys. Rev. Lett.* **86**, 5534 (2001).
- [17] F. Brochard Wyart and J. Daillant, *Can. J. Phys.* **68**, 1084 (1990).
- [18] G. Reiter, *Phys. Rev. Lett.* **68**, 75 (1992).
- [19] U. Thiele, M. Mertig, and W. Pompe, *Phys. Rev. Lett.* **80**, 2869 (1998).
- [20] T. Stange and D. Evans, *Langmuir* **13**, 4459 (1997).
- [21] U. Thiele, M. G. Velarde, and K. Neuffer, *Phys. Rev. Lett.* **87**, 016104 (2001).
- [22] X. Hu, D. Cahill, and R. Averback, *Appl. Phys. Lett.* **76**, 3215 (2000).
- [23] X. Hu, D. G. Cahill, and R. S. Averback, *J. Appl. Phys.* **89**, 7777 (2001).
- [24] J. Bischof, D. Scherer, S. Herminghaus, and P. Leiderer, *Phys. Rev. Lett.* **77**, 1536 (1996).
- [25] J. Bischof, M. Reinmuth, J. Boneberg, S. Herminghaus, T. Palberg, and P. Leiderer (SPIE, 1996), vol. 2777, pp. 119–127.
- [26] S. Herminghaus, K. Jacobs, K. Mecke, J. Bischof, A. Fery, M. Ibn-Elhaj, and S. Schlagowski, *Science* **282**, 916 (1998).
- [27] C. Favazza, J. Trice, H. Krishna, and R. Kalyanaraman, in *Mat. Res. Soc. Symp. Proc.* (Pittsburgh, PA, 2006), vol. 890, pp. 0890–Y04–06.1–06.6.
- [28] C. Favazza, J. Trice, A. Gangopadhyay, H. Garcia, R. Sureshkumar, and R. Kalyanaraman, *J. Elec. Mat.* **35**, 1618 (2006).
- [29] C. Favazza, J. Trice, H. Krishna, R. Kalyanaraman, and R. Sureshkumar, *Appl. Phys. Lett.* **88**, 1531181 (2006).
- [30] C. Favazza, R. Kalyanaraman, and R. Sureshkumar, *Nanotechnology* **17**, 4229 (2006).
- [31] M. von Allmen, *Laser-beam interactions with materials: Physical principles and applications*, vol. 2 of *Springer series in materials science* (Springer-Verlag, Berlin, 1987).
- [32] D. Bäuerle, *Laser Processing and Chemistry* (Springer-Verlag, Berlin, 1996).

- [33] E. Matthias, M. Reichling, J. Siegel, O. W. Kading, S. Petzoldt, H. Skurk, P. Bizenberger, and E. Neske, *Appl. Phys. A* **58**, 129 (1994).
- [34] S. J. Henley, J. D. Carey, and S. R. P. Silva, *Phys. Rev. B* **72**, 195408 (2005).
- [35] B. Yilbas and S. Shuja, *J. Phys. D: Appl. Phys.* **32**, 1947 (1999).
- [36] R. Ram-Mohan, *Finite Element and Boundary Element Applications in Quantum Mechanics* (Oxford University Press, Oxford, 2002).
- [37] O. S. Heavens, *Optical properties of thin solid* (Butterworth Publications, LTD., London, 1955), pp. 76–77.
- [38] V. Voller and C. Prakash, *Int J. Heat Mass Transfer* **30**, 1709 (1987).
- [39] R. Lewis, P. Nithiarasu, and K. Seetharamu, *Fundamentals of the Finite Element Method for Heat and Fluid Flow* (John Wiley and Sons, Ltd., West Sussex, England, 2004).
- [40] S. Henley, J. Carey, and S. Silva, *Phys. Rev. B* **72** (2005).
- [41] J. H. Weaver, C. Kafka, D. W. Lunch, and E. E. Koch, *Physics data, optical properties of metals*, 18 (ISSN 0344-8401) (Fachinformationszentrum Energie, Physik, Matematik G.m.b.H., Karlsruhe, 1981).
- [42] C. Zhang and R. Kalyanaraman, *App. Phys. Lett.* **83**, 4827 (2003).
- [43] W. Zhang, C. Zhang, and R. Kalyanaraman, *J. Vac. Sci. Tech. B* **23**, L5 (2005).
- [44] P.-G. de Gennes, F. Brochard-Wyart, and D. Quere, *Capillarity and Wetting Phenomenon* (Springer, New York, 2003).
- [45] J. Israelachvili, *Intermolecular and surface forces* (Academic Press, London, UK, 1992), chap. van der Waals forces between surfaces.
- [46] R. French, *J. Amer. Ceram. Soc.* **83**, 2117 (2000).
- [47] C. Zhang and R. Kalyanaraman, *J. Mater. Res.* **19**, 595 (2004).
- [48] D. Linde, ed., *The CRC Handbook of Chemistry and Physics* (CRC Press, Boca Raton, 1992).
- [49] N. Bansal and R. Doremus, *Handbook of glass properties* (Academic Press, Inc., Orlando, Florida, 1986).
- [50] R. Tyagi and R. Mathur, *J. Phys. D.* **3**, 1811 (1970).
- [51] S. Montague, C. Draper, and G. Rosenblatt, *J. Phys. Chem. Solids* **40**, 987 (1979).

Table Captions

- Table I: Material and scaling parameters (T-dependent and T-independent) used in modeling.
- Table II: Coefficients for linear fits of liquid lifetime obtained from modeling.
- Table III: Coefficients of linear fits for peak temperature obtained from modeling.
- Table IV: Linear fitting parameters for heating portion of thermal cycles.
- Table V: Exponential Fitting parameters for cooling portion of thermal cycle.
- Table VI: Temperature dependence of liquid Co material parameters.

Figure Captions

- Figure 1: (a) Schematic diagram for modeling of laser heating of a metallic nanolayer on a semi-infinite insulating substrate. (b) Plot of thickness-dependence of reflectivity R of Co/SiO₂ bilayer estimated from Ref. [37].
- Figure 2: Thermal behavior of the Co film on SiO₂ irradiated by a pulsed laser. (a) Time-dependent temperature obtained for the analytic and numerical model using temperature independent parameters. The symbols are from the analytical model while the lines are from the numerical calculations. (b) Numerical results incorporating the phase change and T-dependent parameters for various film thickness. (c) Laser energy density threshold for melting E_m of Co films on SiO₂. Comparison of experimental measurement (solid circles) with calculations from our analytical model (solid line) and numerical model (dashed line).
- Figure 3: (a) Analytical form of the heating portion of thermal cycle for 3 nm Co on SiO₂ showing a linear increase in liquid temperature with increasing laser energy density. (b) Analytical form of the cooling portion of thermal cycle for 3 nm Co on SiO₂ showing a fit using a second order exponential function. Cumulative results of the analytical (closed symbols) and numerical model (open symbols) using T-dependent materials parameters: (c) liquid lifetime vs. laser energy density; and (d) peak temperature vs. laser energy density. Closed symbols are analytical results while the open symbols are from numerical calculations.
- Figure 4: Dewetting pattern evolution in a 2 nm Co film irradiated at 200 mJ/cm² as a function of number of pulses n . The top row are SEM images while the bottom row show corresponding power spectrum. (a) $n=10$; (b) $n = 100$; (c) $n = 1000$; (d) $n = 10500$. All the power spectra have an annular structure indicating a band of spatial frequencies implying short range spatial order.
- Figure 5: Dewetting pattern evolution in a 2 nm Co film irradiated as a function of laser energy density for irradiation by 100 pulses. (a) 190 mJ/cm²; (b) 200 mJ/cm²; (c) 220 mJ/cm²; (d) 250 mJ/cm².
- Figure 6: Dewetting pattern evolution in a 4.4 nm Co film irradiated at 93 mJ/cm² as a function of number of pulses n . The top row are SEM images while the bottom row show corresponding power spectrum. (a) $n=10$; (b) $n = 100$; (c) $n = 1000$; (d) $n = 10500$. Similar to the results for the 2 nm film, all the power spectra have an annular structure indicating a band of spatial frequencies implying short range spatial order.

- Figure 7: Monomodal size distribution and average diameter of nanoparticles in the final robust state of laser-induced dewetting. (a) An average diameter of 38 nm results for the 2 nm Co film; (b) Average diameter of 207 nm for the 4.4 nm Co film.
- Figure 8: Quantitative analysis of the spatial frequencies resulting from the short range order in the dewetting patterns for the 4.4 nm Co film. (a) The radial distribution function $g(k)$ for the patterns of fig. 6 showing an initial increase as the holes expand and then a decrease as the nanoparticles start to form. (b) Behavior of the characteristic length extracted from the peak in the $g(k)$ as a function of irradiation time n at various laser energies. The spacing of the final state is independent of the laser energy.
- Figure 9: Analysis of the various length scales in the final robust nanoparticle state as a function of film thickness. (a) The average nearest-neighbour spacing R of nanoparticles; (b) The average nanoparticle diameter D ; (c) The average areal density of nanoparticles in $\#/cm^2$. The fits show exponents in good agreement with linear spinodal dewetting theory. The R^2 values in each graph indicate the correlation coefficient of the least-squares fitting.
- Figure 10: Role of temperature on the ripening rate of dewetting. (a) A linear dependence of the spinodal ripening rate is predicted from the temperature dependence of the Co liquid material parameters (Table. VI). (b) The experimentally observed ripening rate L/n for various film thickness and energies. The symbols are experimental data while the dashed lines are linear fits.

Quantity	Description	Value/Expression	Reference
E_o	laser energy density	$98 - 700 \frac{mJ}{cm^2}$	
t_p	pulse duration	9 ns	[47]
$\sigma = \frac{t_p}{2 \cdot \sqrt{2 \cdot \ln(2)}}$	standard deviation	3.822 ns	
$R(h)$	thickness-dependent reflectivity	$R_{SiO_2} \leq R \leq R_{Co}$	[37, 41]
a_m	absorbtivity	$9.21 \cdot 10^7 \text{ cm}^{-1}$	[41]
L	heat of transformation	$274 \frac{J}{g}$ for Co	[48]
T_m	melting temperature	1768 K for Co	[48]
ρ_m	metal film density	$(8.9 \cdot (1 - H(T - T_m)) + 7.75 \cdot H(T - T_m)) \cdot \frac{g}{cm^3}$	[48]
ρ_s	substrate density	$2.2 \frac{g}{cm^3}$	[49]
$(C_{eff})_m$	temperature dependent film heat capacity	$(0.42 \cdot (H(T) - H(T - T_m)) + 0.59 \cdot H(T - T_m)) \frac{J}{g \cdot K}$	[48]
	temperature independent film heat capacity	$0.42 \frac{J}{g \cdot K}$	[48]
$(C_{eff})_s$	temperature dependent substrate heat capacity	$(0.931 + (2.56 \cdot 10^{-4}) \cdot T - 0.240/T^2) \frac{J}{g \cdot K}$	[49]
	temperature independent substrate heat capacity	$0.937 \frac{J}{g \cdot K}$	[49]
k_m	temperature dependent film thermal conductivity	$(0.0912 + 264.65/T) \cdot (H(T) - H(T - 1000)) + (-0.0016 \cdot T + 2.4402) \cdot (H(T - 1000) - H(T - 1400)) \frac{W}{cmK}$	[50, 51]
	temperature independent film thermal conductivity	$1 \frac{W}{cmK}$	[48]
k_s	substrate thermal conductivity	$0.014 \frac{W}{cmK}$	[49]
ζ	analytic model scaling factor	0.76	
β	numeric model scaling factor	10^{-3}	
ϵ	phase change tuning parameter	$15K$	
T_o	room temperature	$300K$	
h	film thickness	$1 - 11 \text{ nm}$	

Table I:

$h(\text{nm})$	Model Used	$A(h_m) (ns \cdot cm^2/mJ)$	$B(h_m) (ns)$
1	Numercial	0.070 ± 0.002	-21.91 ± 0.78
	Analytic	0.074 ± 0.003	-22.10 ± 1.16
2	Numerical	0.117 ± 0.006	-18.86 ± 1.28
	Analytic	0.122 ± 0.008	-19.23 ± 1.59
3	Numercial	0.144 ± 0.009	-16.04 ± 1.46
	Analytic	0.150 ± 0.009	-16.61 ± 1.48
5	Numercial	0.217 ± 0.019	-17.29 ± 2.19
	Analytic	0.210 ± 0.012	-16.4 ± 1.36
11	Numercial	0.301 ± 0.016	-17.18 ± 1.45
	Analytic	0.294 ± 0.016	-17.21 ± 1.36

Table II:

$h_m(nm)$	Model Used	$C(h_m)(K \cdot cm^2/mJ)$	$D(h_m)(K)$
1	Numercial	2.32 ± 0.0283	362.6 ± 18.2
	Analytic	2.57 ± 0.017	301.6 ± 11.2
3	Numercial	5.69 ± 0.13	461.3 ± 35.39
	Analytic	6.8 ± 0.0	294 ± 0.0
5	Numercial	9.28 ± 0.26	271 ± 48.6
	Analytic	9.95 ± 0.013	300.6 ± 2.43
11	Numercial	14.47 ± 0.75	21.05 ± 94.4
	Analytic	15.3 ± 0.0	301 ± 0.0

Table III:

$h(nm)$	$E(mJ/cm^2)$	$R(h)(K/ns)$	$S(h)(K)$
1	380	152.693 ± 13.1	164.071 ± 105.69
2	200	142.571 ± 10.2	209.13 ± 77
3	150	153.446 ± 12.059	143.304 ± 99.2132
5	110	158.161 ± 12.0328	122.018 ± 97.011
11	90	171.911 ± 11.7928	66.9107 ± 95.0725

Table IV:

$h(nm)$	E (mJ/cm^2)	$A_1(h)(K)$	$t_1(ns)$	$A_2(h)(K)$	$t_2(ns)$	$y_o(K)$
1	380	592.198 ± 5.364	71.77 ± 0.0003	5385 ± 46.1912	3.998 ± 0.0009	502.4655 ± 2.997
2	200	504.02 ± 1.96522	128.137 ± 0.0001	5104.876 ± 26.729	8.5445 ± 0.0004	433.05278 ± 0.9292
3	150	552.6079 ± 28.0724	124.828 ± 0.0001	5282.71 ± 28.072	8.5449 ± 0.0004	425.43695 ± 0.7664
5	110	549.15 ± 1.95676	139.596 ± 0.0000	4979.213 ± 22.6219	9.15733 ± 0.0003	434.05965 ± 0.45438
11	90	595.3555 ± 1.60323	188.619 ± 0.000	4358.470 ± 14.7928	10.9719 ± 0.0002	430.46041 ± 0.40428

Table V:

Property	Value
$\gamma(T = T_{mp})$	$1.88 \text{ } Jm^{-2}$
γ_T	$-0.5 \times 10^{-3} \text{ } Jm^{-2} K^{-1}$
$\eta(T)$	$0.3272 \times 10^{-3} e^{\frac{0.3742 \times 10^5}{RT}} \text{ } Pa - s$
η_T	$\frac{-4500.8}{T^2} \eta(T) \text{ } Pa - s - K^{-1}$

Table VI:

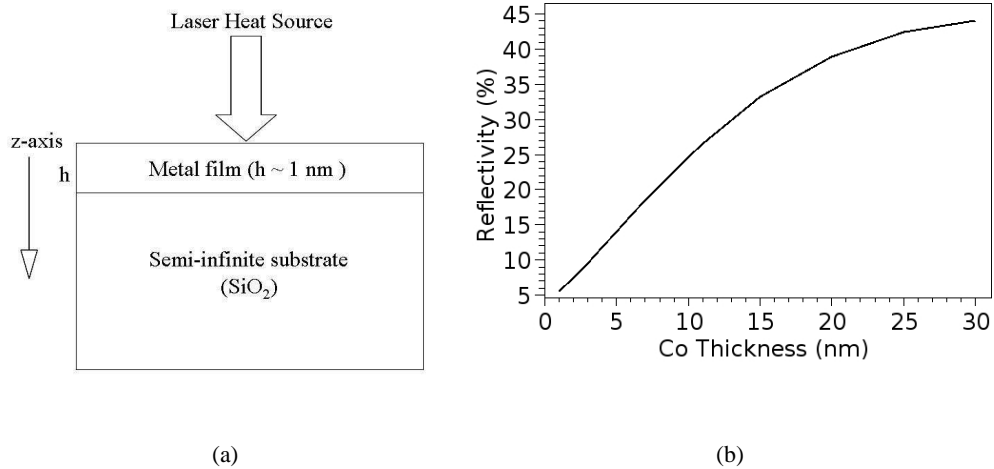
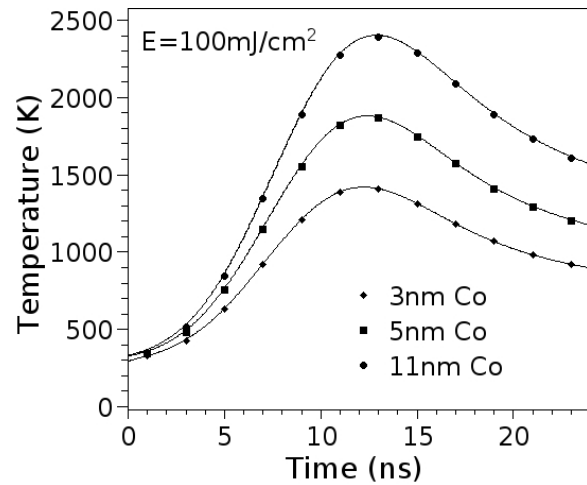
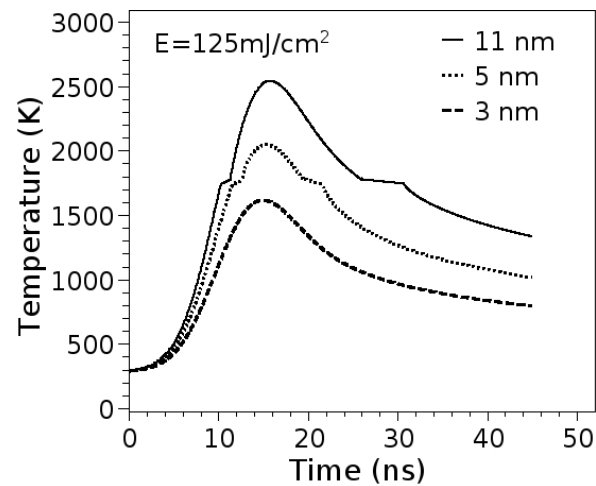


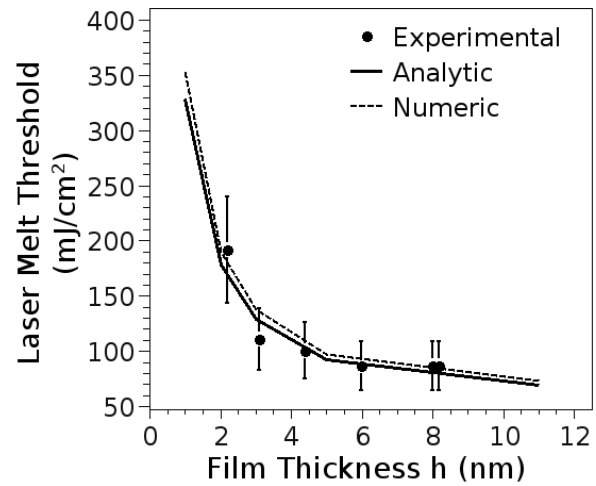
Figure 1:



(a)



(b)



(c)

Figure 2:

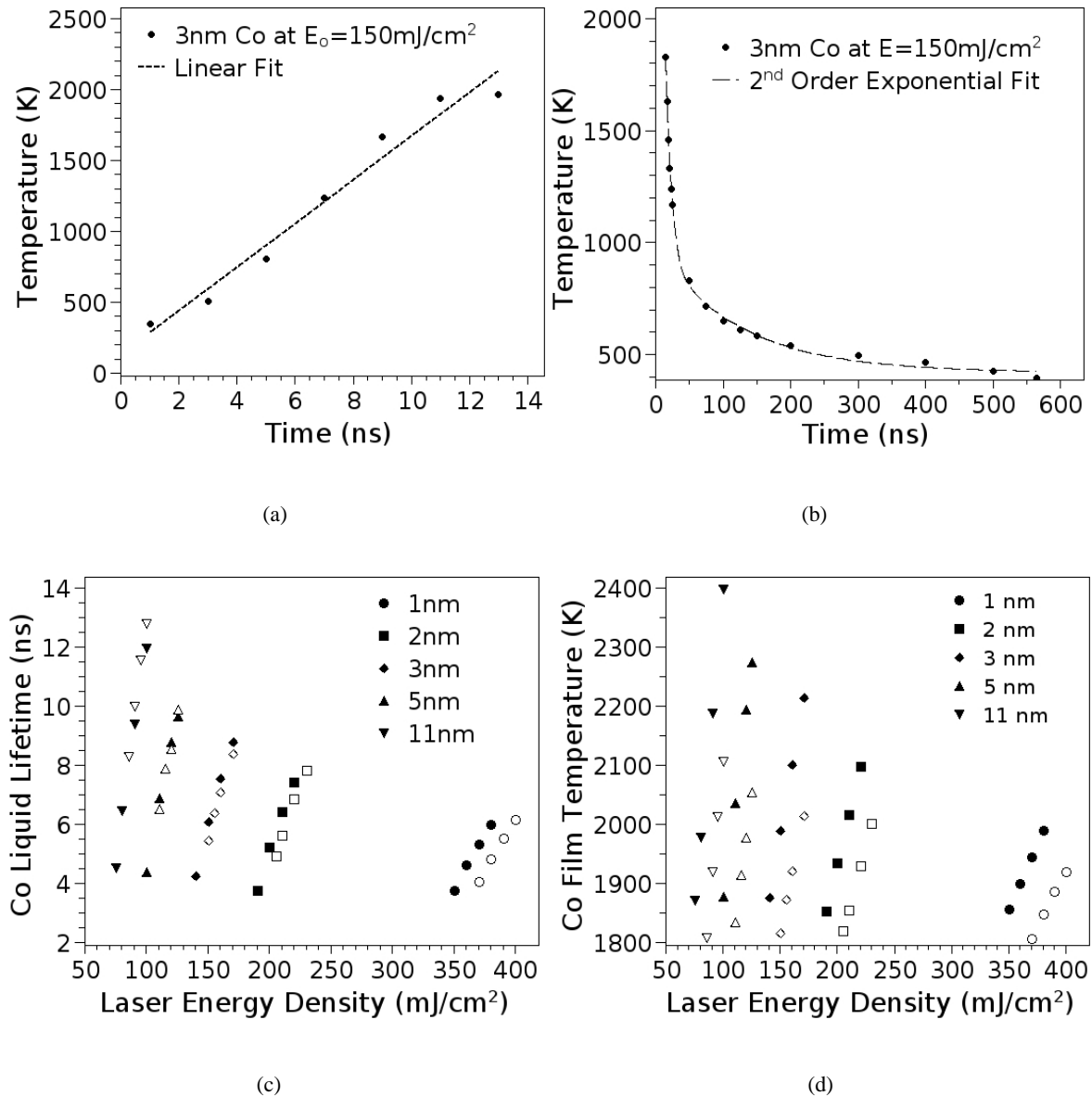


Figure 3:

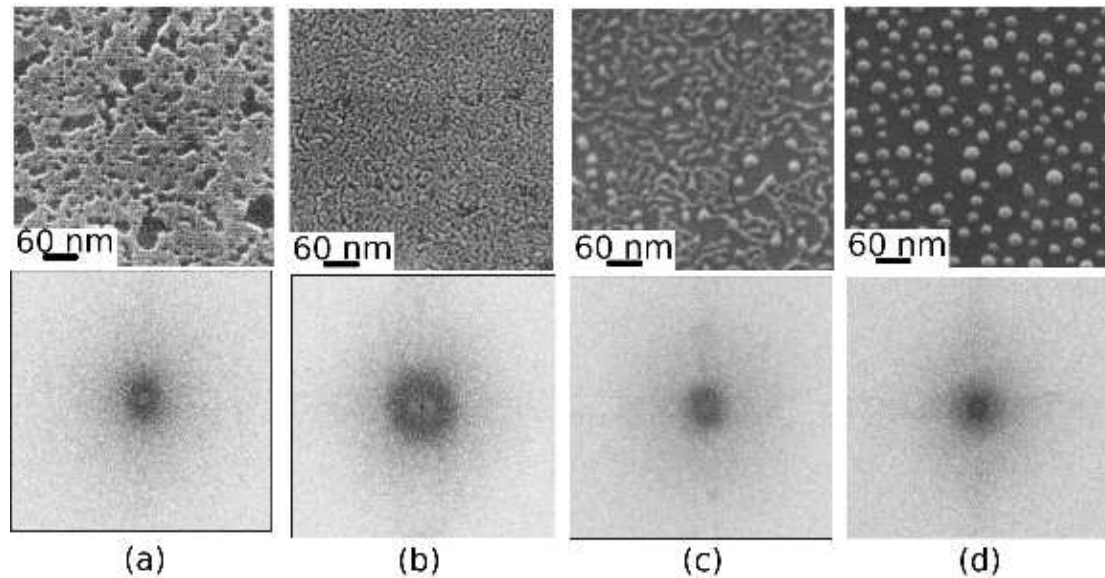


Figure 4:

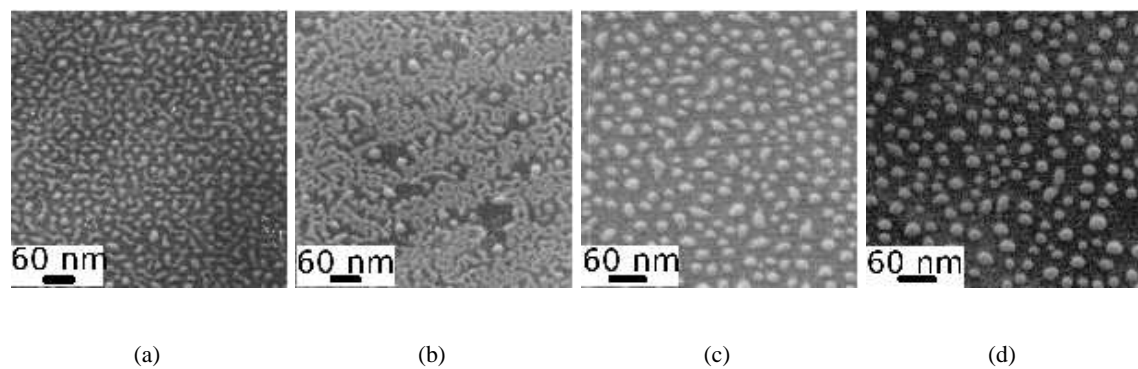


Figure 5:

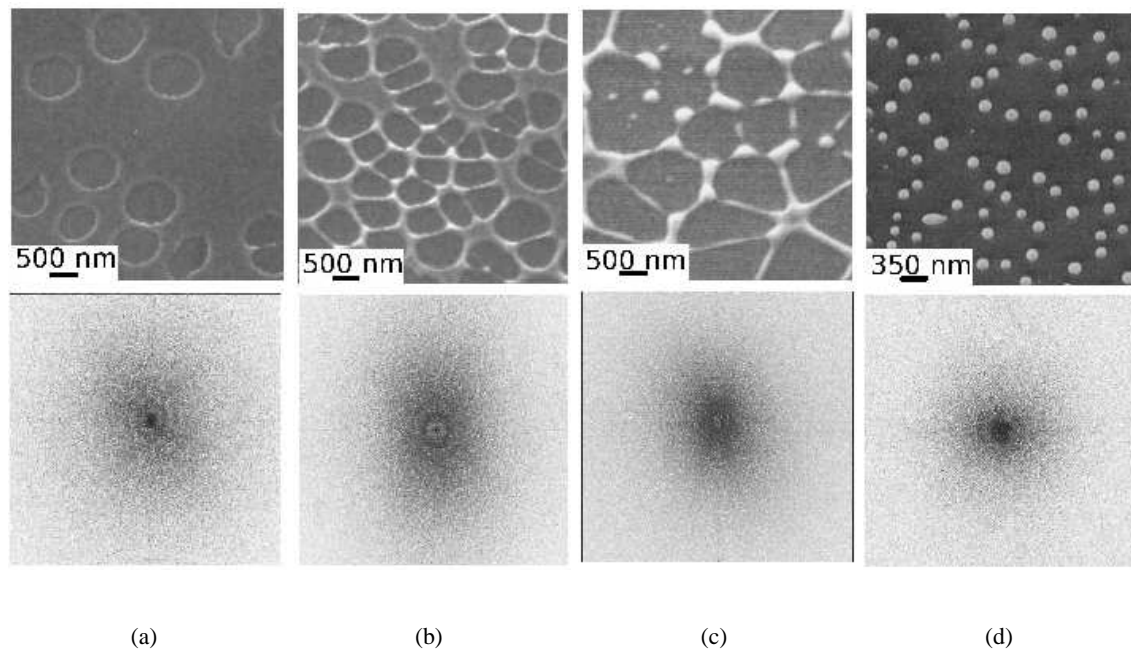


Figure 6:

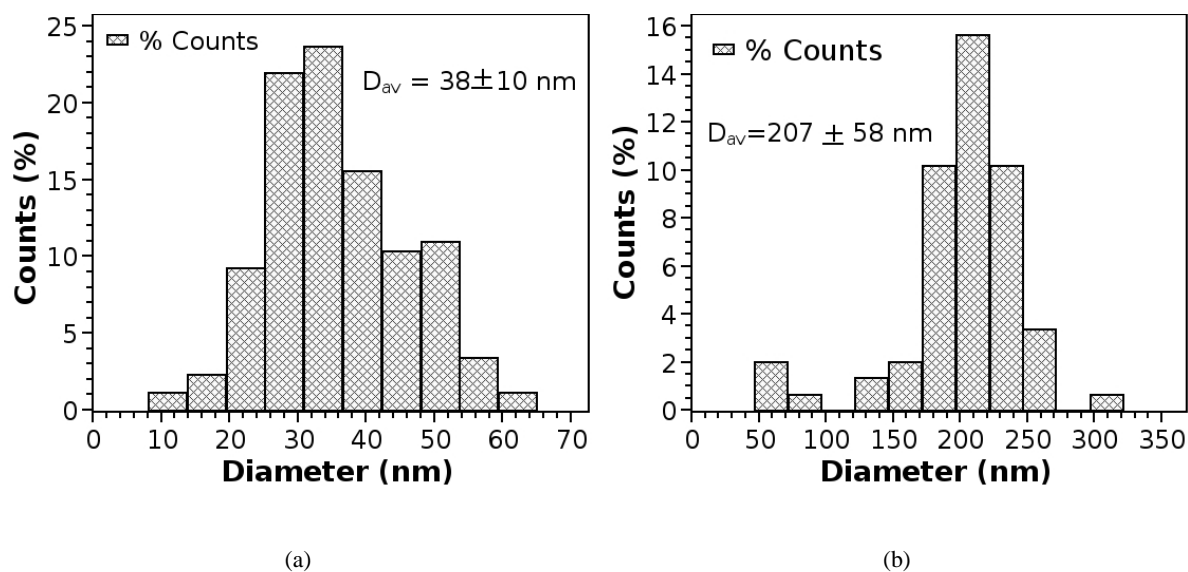


Figure 7:

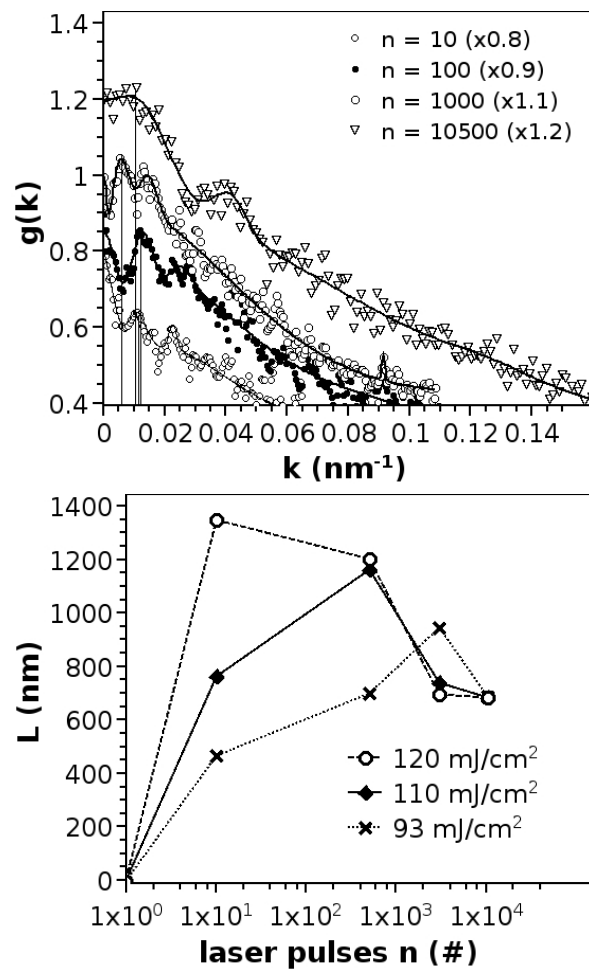


Figure 8:

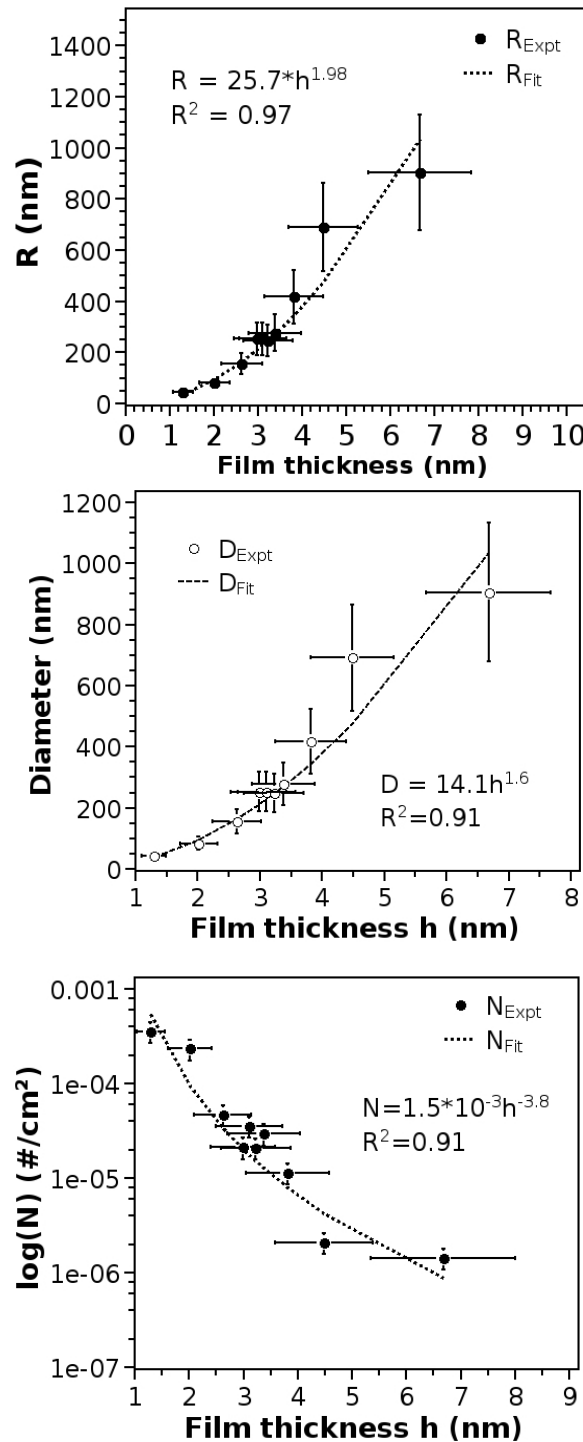


Figure 9:

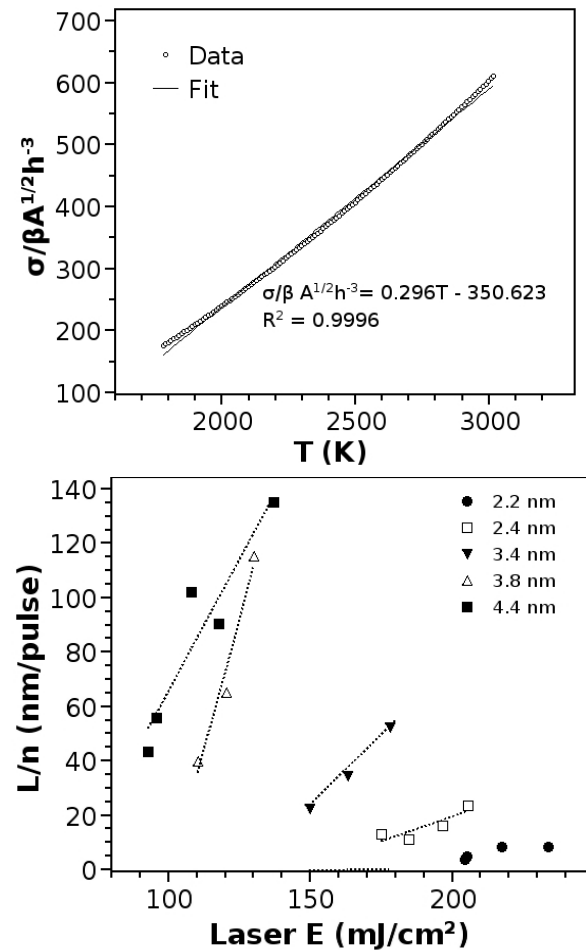


Figure 10: